



Delayed fluorescence from a zirconium(IV) photosensitizer with ligand-to-metal charge-transfer excited states

Yu Zhang¹, Tia S. Lee², Joseph M. Favale³, Dylan C. Leary¹, Jeffrey L. Petersen¹, Gregory D. Scholes², Felix N. Castellano³ and Carsten Milsmann¹✉

Advances in chemical control of the photophysical properties of transition-metal complexes are revolutionizing a wide range of technologies, particularly photocatalysis and light-emitting diodes, but they rely heavily on molecules containing precious metals such as ruthenium and iridium. Although the application of earth-abundant ‘early’ transition metals in photosensitizers is clearly advantageous, a detailed understanding of excited states with ligand-to-metal charge transfer (LMCT) character is paramount to account for their distinct electron configurations. Here we report an air- and moisture-stable, visible light-absorbing Zr(IV) photosensitizer, Zr(MesPDPPh)₂, where [MesPDPPh]²⁻ is the doubly deprotonated form of [2,6-bis(5-(2,4,6-trimethylphenyl)-3-phenyl-1H-pyrrol-2-yl)pyridine]. This molecule has an exceptionally long-lived triplet LMCT excited state ($\tau = 350 \mu\text{s}$), featuring highly efficient photoluminescence emission ($\Phi = 0.45$) due to thermally activated delayed fluorescence emanating from the higher-lying singlet configuration with significant LMCT contributions. Zr(MesPDPPh)₂ engages in numerous photoredox catalytic processes and triplet energy transfer. Our investigation provides a blueprint for future photosensitizer development featuring early transition metals and excited states with significant LMCT contributions.

Photoluminescent transition-metal complexes are critical components in a diverse range of important scientific applications, including solar energy conversion^{1–3}, photocatalysis^{4–6}, photodynamic therapy⁷ and organic light-emitting diodes (OLEDs)^{8,9}. A universal requirement for the generation of suitably long-lived molecular excited states for such applications is rapid intersystem crossing between excited-state manifolds of different spin multiplicity, most commonly represented by the population of triplet excited states in molecules with diamagnetic ground states. Spin-forbidden radiative relaxation from the triplet state to the ground state is sufficiently slow to harness the energy stored in the excited state for intermolecular electronic energy or single-electron transfer chemistry with suitable substrates. For most traditional transition-metal chromophores, radiative relaxation of long-lived excited states in the absence of quenchers occurs through phosphorescence, that is, direct transition between the lowest-energy triplet state and the diamagnetic ground state. A second, less common pathway is thermally activated delayed fluorescence (TADF)¹⁰, which involves reverse intersystem crossing from a long-lived triplet back to the singlet excited state, facilitated by a small energy separation between these states that is easily surmounted by the available thermal energy (typically $<0.2 \text{ eV}$)¹¹. Over the past decade, TADF has emerged as an important design principle for the development of new photo- and electroluminescent molecules, but has almost exclusively been applied in the field of organic luminophores^{12,13} and Cu(I)-based photosensitizers^{14–16}. Here, we demonstrate the successful leveraging of TADF in the construction of a long-lived and high-quantum-yield photoluminescent early-transition-metal complex based on Zr(IV), featuring a $4d^0$ configuration and excited states with significant ligand-to-metal charge transfer (LMCT) contributions.

Group III to V transition metals are attractive candidates for the development of earth-abundant and environmentally benign alternatives to the more prevalent precious-metal chromophores¹⁷. Their natural abundance often rivals that of first-row late transition metals such as Fe^{18–20} and Cu^{21,22}. The group IV elements, featuring Ti and Zr as the second and fourth most earth-abundant transition metals, respectively, are particularly interesting because they would allow the design of readily scalable yet cost-efficient photoluminescent molecules, but these have rarely been studied in this context. The underlying challenge impeding the use of their excited states lies in the fundamentally distinct electronic structures that impart deleterious photophysical and (photo)chemical properties and require alternative strategies compared to those well-established for late transition metals²³. Most importantly, electron-deficient d^0 early transition metals require a reversal of the initial intramolecular charge transfer step from metal-to-ligand charge transfer (MLCT) to LMCT. This can be achieved by combining the electron-deficient metal with carefully designed electron-rich ligand systems, effectively resulting in a role reversal of electron donor and electron acceptor compared to traditional late-transition-metal chromophores. Although this approach has recently been applied to substantially improve the photophysical properties of photoluminescent iron(III) complexes^{19,20}, a natural benefit of metals with d^0 configurations is the lack of metal-centred excited states that often lead to reduced emission lifetimes and quantum yields in late-transition-metal chromophores. Despite these seemingly simple considerations, only a limited number of photoluminescent group III to V complexes have been reported so far, and their short lifetimes do not broadly facilitate photoinduced intermolecular reactions^{24–30}.

Expanding on the few available studies, we recently demonstrated that zirconium complexes with electron-rich pyridinepyrrolide and

¹C. Eugene Bennett Department of Chemistry, West Virginia University, Morgantown, WV, USA. ²Department of Chemistry, Princeton University, Princeton, NY, USA. ³Department of Chemistry, North Carolina State University, Raleigh, NC, USA. ✉e-mail: camilsmann@mail.wvu.edu

pyridinedipyrroliide (PDP) ligands exhibit long-lived photoluminescence from excited states with significant LMCT character and can be utilized as photosensitizers in reductive photoredox reactions^{31–34}. Most notably, $\text{Zr}(\text{MePDP}^{\text{Ph}})_2$ ($\text{H}_2\text{MePDP}^{\text{Ph}}$ = 2,6-bis(5-methyl-3-phenyl-1*H*-pyrrol-2-yl)pyridine) was identified as an attractive alternative to precious-metal photocatalysts due to its remarkably long excited-state lifetime of 325 μs and readily accessible reductive redox chemistry^{31,32}. This proof-of-principle observation signals the opportunity that early-transition-metal chromophores can complement or even surpass the performance of precious-metal photosensitizers. However, several important questions and challenges have remained concerning the fundamental understanding of the photophysical properties, expansion of the ground- and excited-state electron transfer reactivity to include oxidative processes, and the high water sensitivity inherent to zirconium amides. Here, we report a new, benchtop-stable zirconium photosensitizer that can facilitate photoredox reactions via oxidative and reductive photo-induced single-electron transfer or excited-state energy transfer. Temperature-dependent emission studies in combination with picosecond transient absorption (TA) spectroscopy now clearly establish that photoluminescence in $\text{Zr}(\text{PDP})_2$ complexes is dominated by TADF at and around room temperature, which is rare for early-transition-metal complexes or photoluminescent molecules featuring LMCT excited states^{35,36}.

Results and discussion

Synthesis and ground-state characterization. Our studies commenced with the synthesis of $\text{Zr}(\text{MesPDP}^{\text{Ph}})_2$ using a significantly bulkier PDP ligand derived from $\text{H}_2\text{MesPDP}^{\text{Ph}}$ (2,6-bis(5-(2,4,6-trimethylphenyl)-3-phenyl-1*H*-pyrrol-2-yl)pyridine)³⁷ (Fig. 1). In stark contrast to previously studied luminescent zirconium compounds, this complex is remarkably stable over a wide temperature and pH range under ambient conditions due to the improved steric protection of the metal centre. Only minimal signs of decomposition were observed on heating the compound in refluxing mesitylene solution or on addition of concentrated mineral acids to tetrahydrofuran (THF) solutions of $\text{Zr}(\text{MesPDP}^{\text{Ph}})_2$ at room temperature (Supplementary Fig. 9). Single-crystal X-ray diffraction analysis (Fig. 1) and ^1H and $^{13}\text{C}\{^1\text{H}\}$ NMR spectroscopy (Supplementary Figs. 3 and 4) respectively established a rigid D_{2d} symmetric structure for $\text{Zr}(\text{MesPDP}^{\text{Ph}})_2$ in the solid state and solution. A key feature of the molecular structure is the sandwich-type stacking between the central pyridine ring of each $\text{MesPDP}^{\text{Ph}}$ ligand and the two mesityl substituents of the second ligand with short distances of 3.4–3.7 Å between the π systems (Supplementary Fig. 1). These interactions increase the overall rigidity of the molecular structure and contribute to the favourable photophysical and electrochemical properties of the complex (vide infra). Furthermore, the large steric profile of the bulky mesityl substituents prevents any access to the strongly basic nitrogen atoms of the pyrroliide rings and the electrophilic zirconium centre, which rationalizes the unusual stability of $\text{Zr}(\text{MesPDP}^{\text{Ph}})_2$ towards hydrolysis (Supplementary Fig. 2).

Cyclic voltammetry using ferrocene as an internal reference (Fig. 2) revealed that $\text{Zr}(\text{MesPDP}^{\text{Ph}})_2$ retains the one-electron reduction events ($E_{1/2} = -2.25$ and -2.95 V) previously established for $\text{Zr}(\text{MePDP}^{\text{Ph}})_2$ (ref. 32), but provides additional access to reversible oxidative redox events ($E_{1/2} = 0.53$ and 0.82 V). As expected for a $\text{Zr}(\text{IV})$ compound, density functional theory (DFT) calculations illustrate that these oxidations are exclusively ligand-centred (Supplementary Fig. 37), which suggests that the improved protection of the PDP π systems in $\text{Zr}(\text{MesPDP}^{\text{Ph}})_2$ prevents otherwise detrimental pyrrolyl radical chemistry³⁸. Redox titrations with sodium naphthalenide (Supplementary Fig. 7) and thianthrenium tetrafluoroborate (Supplementary Fig. 8) provided access to the one-electron reduced and oxidized complexes in solution, respectively. A comparison of the electronic absorption spectra for $[\text{Zr}(\text{MesPDP}^{\text{Ph}})_2]^n$ ($n = 1+, 0, 1-$) is provided in Fig. 2.

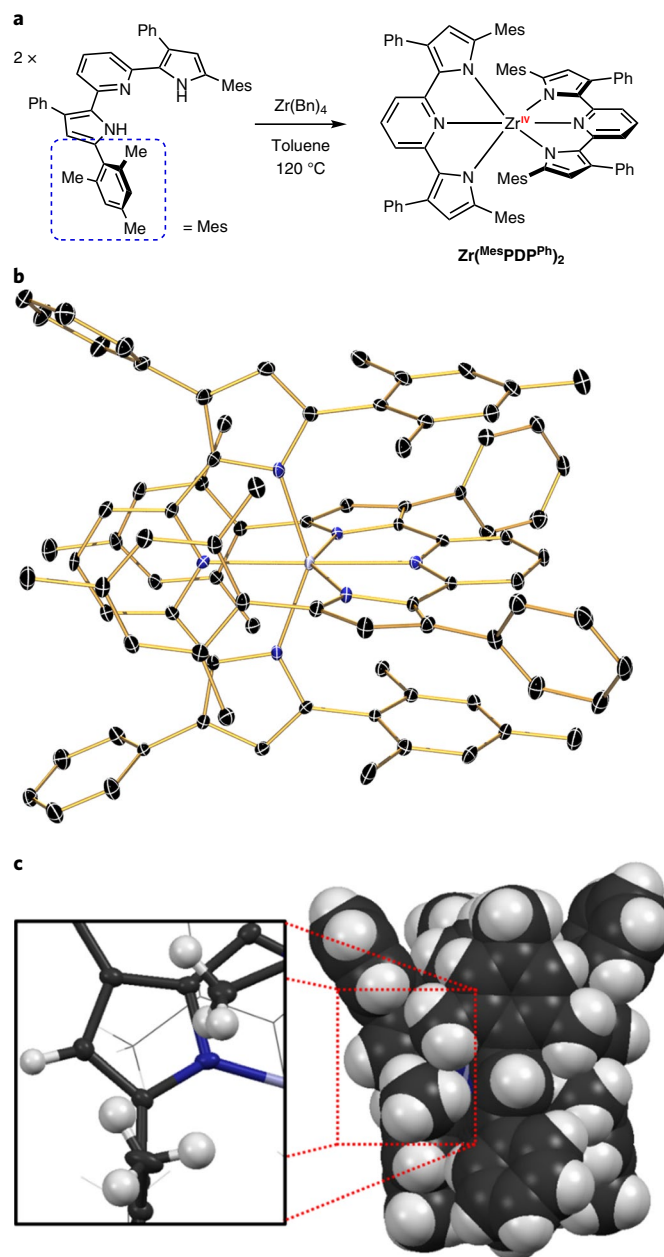


Fig. 1 | Synthesis and structural characterization of $\text{Zr}(\text{MesPDP}^{\text{Ph}})_2$.

a, Synthesis of $\text{Zr}(\text{MesPDP}^{\text{Ph}})_2$. **b**, Molecular structure shown with 30% probability ellipsoids obtained via X-ray diffraction. Hydrogen atoms are omitted for clarity. **c**, Space-filling model highlighting the tight packing of the mesityl substituents and the resulting steric protection of the Zr–N bonds responsible for the increased air and moisture stability of the complex. The inset shows the positioning of the methyl groups above and below the 2- and 5-positions of the pyrrole rings. This motif blocks access to the reactive pyrrolyl radical moieties formed upon oxidation of the complex and enables reversible single-electron transfer under oxidative conditions.

Room-temperature absorption and emission profiles. The electronic absorption spectrum of $\text{Zr}(\text{MesPDP}^{\text{Ph}})_2$ in THF (Fig. 2) is very similar to that reported for $\text{Zr}(\text{MePDP}^{\text{Ph}})_2$, indicating that the change from methyl to mesityl substituents does not significantly perturb the electronic structure of the $\text{Zr}(\text{PDP})_2$ core. This is supported by DFT calculations, which show that the pyrrole substituents exert

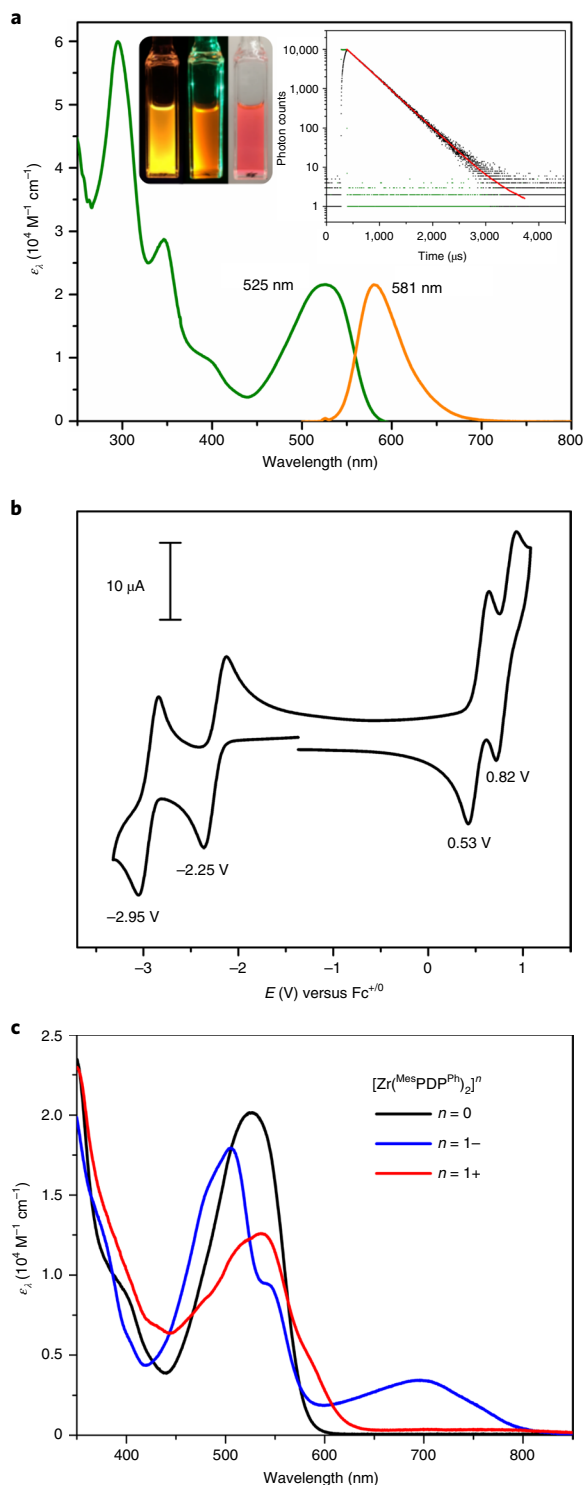


Fig. 2 | Electrochemical and optical properties of $\text{Zr}(\text{MesPDP}^{\text{Ph}})_2$.

a, Electronic absorption and emission spectra in THF under a nitrogen atmosphere. The insets show THF solutions of $\text{Zr}(\text{MesPDP}^{\text{Ph}})_2$ under ultraviolet (UV; 254 nm), green (LED; 530 nm) and ambient light irradiation (left) and photoluminescence decay ($\tau_{\text{PL}} = 350 \pm 10 \mu\text{s}$) obtained via time-correlated single photon counting (right). **b**, Cyclic voltammogram recorded in THF at room temperature using the ferrocenium/ferrocene ($\text{Fc}^{+/0}$) couple as the reference. These electrochemical data clearly establish multiple fully reversible oxidation and reduction events. **c**, Comparison of the electronic absorption spectra for the one-electron reduced (blue) and oxidized (red) species and the neutral starting material (black), obtained from redox titrations.

only very minor contributions to the frontier molecular orbitals in the ground state (Supplementary Fig. 38). Based on time-dependent DFT (TD-DFT) calculations, the strong absorption band in the visible region ($\lambda_{\text{max}} = 525 \text{ nm}$, $\epsilon_{525} = 21,570 \text{ M}^{-1} \text{ cm}^{-1}$) can be assigned to mixed singlet intra-ligand (^1IL)/ $^1\text{LMCT}$ transitions having 40% LMCT character. The absence of solvatochromism, evident from the near identical spectra in solvents of varying polarity (Supplementary Figs. 10 and 11), suggests that the electronic dipole moment of the molecule does not change on excitation. Given that $\text{Zr}(\text{MesPDP}^{\text{Ph}})_2$ has no dipole moment in the ground state due to its D_{2d} symmetry, the initial state generated via $^1\text{IL}/^1\text{LMCT}$ excitation must be delocalized symmetrically over both PDP ligands. This is again supported by TD-DFT calculations, which identify the degenerate pair of lowest unoccupied molecular orbitals (LUMOs) calculated for the ground state as the main acceptor orbitals for the transitions in the visible region. As previously reported for $\text{Zr}(\text{MePDP}^{\text{Ph}})_2$ (refs. ^{31,32}), these orbitals are fully delocalized over the zirconium centre and both PDP ligands.

Excitation of $\text{Zr}(\text{MesPDP}^{\text{Ph}})_2$ in solution at room temperature with UV or visible light below 600 nm induced strong and remarkably long-lived photoluminescence. The steady-state emission spectrum (Fig. 2) exhibits a single broad band with a maximum at 581 nm, independent of the solvent. Regardless of the excitation wavelength, the spectral profile mirrors the lowest-energy $^1\text{IL}/^1\text{LMCT}$ absorption band and exhibits no fine structure. The emission maximum is blueshifted by 14 nm (405 cm^{-1}) compared to that reported for $\text{Zr}(\text{MePDP}^{\text{Ph}})_2$ ($\lambda_{\text{max}} = 595 \text{ nm}$)^{31,32}, resulting in a smaller Stokes shift. Additionally, the emission peak width is decreased for $\text{Zr}(\text{MesPDP}^{\text{Ph}})_2$ (full-width at half-maximum (FWHM) = $1,610 \text{ cm}^{-1}$) compared to $\text{Zr}(\text{MePDP}^{\text{Ph}})_2$ (FWHM = $2,160 \text{ cm}^{-1}$). Considering the negligible electronic effects of the different pyrrole substituents discussed above, these observations are consistent with reduced vibrational relaxation due to the more rigid structure of $\text{Zr}(\text{MesPDP}^{\text{Ph}})_2$. Further supporting this hypothesis, the emission quantum yield determined for $\text{Zr}(\text{MesPDP}^{\text{Ph}})_2$ by the comparative method in deaerated THF solution at room temperature ($\Phi_{\text{PL}} = 0.45$) is increased to more than fivefold compared to $\text{Zr}(\text{MePDP}^{\text{Ph}})_2$ ($\Phi_{\text{PL}} = 0.08$). Similar improvements in quantum yield through rigidification of the ligand scaffold were recently reported for earth-abundant Mo MLCT photosensitizers³⁹. The emission decay kinetics determined under the same conditions using time-correlated single photon counting (TCSPC) exhibits single-exponential behaviour with a lifetime of $\tau_{\text{PL}} = 350 \pm 10 \mu\text{s}$.

Temperature-dependent emission studies. The photoluminescence characteristics of $\text{Zr}(\text{MesPDP}^{\text{Ph}})_2$ are highly sensitive to variation in temperature. The temperature-dependent emission profiles recorded in 2-MeTHF (Fig. 3) reveal a steady decrease in the emission intensity with decreasing temperature. Although only minor changes to the overall shape of the emission band are visible in the range from 60°C to -20°C , a second emission band with a maximum at 642 nm becomes apparent as a shoulder at lower temperatures. On reaching -130°C , the lowest temperature still maintaining a fluid solution, this feature is clearly resolved and dominates the emission spectrum, while the band centred at 581 nm has almost completely vanished. This behaviour is indicative of photoluminescence from two distinct excited states separated energetically by $\sim 1,640 \text{ cm}^{-1}$ based on the difference between the peak maxima of the two bands. The small energy gap between these two states, assigned as S_1 and T_1 , is within the thermally accessible range and is consistent with a TADF mechanism. Following rapid intersystem crossing, emission at low temperatures occurs primarily through phosphorescence from the lower-energy T_1 state, because reverse intersystem crossing to the higher-energy S_1 state is no longer thermally accessible. On increasing the temperature, reverse intersystem crossing enables a competing emission process through delayed fluorescence, which becomes

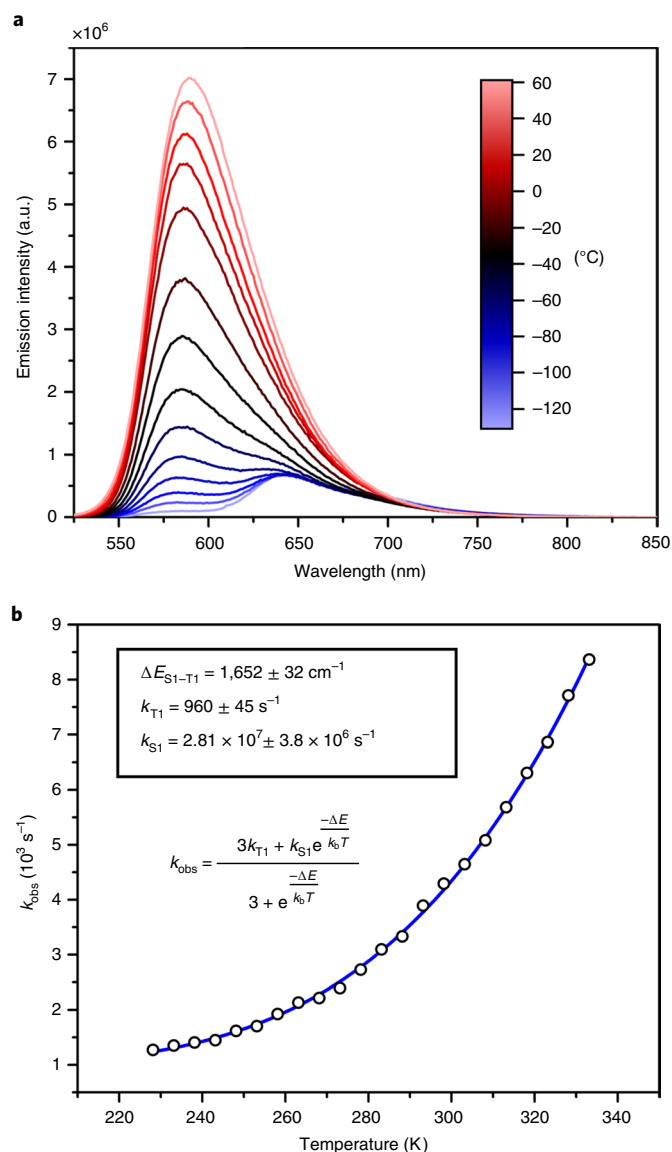


Fig. 3 | Temperature-dependent emission characteristics of $\text{Zr}(\text{MesPDP}^{\text{Ph}})_2$ supporting thermally activated delayed fluorescence. **a**, Temperature-dependent emission spectra recorded in 2-MeTHF under a dinitrogen atmosphere. The two different emission bands observed at high and low temperatures indicate emission from two distinct excited states (S_1 and T_1). The temperature-dependent changes in the emission profile are consistent with variations in the relative occupation of the two states according to their different energies. **b**, Temperature dependence of the photoluminescence rate constant in 2-MeTHF. The blue line represents the best fit of the data using the depicted formula and values for k_{S_1} , k_{T_1} and $\Delta E_{S_1-T_1}$. This model of the data assumes a rapid equilibrium between the S_1 and T_1 states, following a simple Boltzmann distribution.

the dominant radiative pathway under ambient conditions. Aside from the expected redshift between fluorescence and phosphorescence, the emission profiles for both processes in solution are quite similar for $\text{Zr}(\text{MesPDP}^{\text{Ph}})_2$, suggesting that the T_1 state is of similar mixed IL/LMCT character as the S_1 state. This is supported by DFT calculations for the electronic structure of the lowest-energy triplet excited state.

Further insight into the proposed delayed fluorescence process for $\text{Zr}(\text{MesPDP}^{\text{Ph}})_2$ was gained through temperature-dependent emission lifetime measurements (Fig. 3). As anticipated for a TADF

chromophore, the photoluminescence lifetime in fluid 2-MeTHF solution decreases as a function of increasing temperature. The data were readily fit using a kinetic model featuring two emitting states (S_1 and T_1) that are in rapid thermal equilibrium due to a small energy splitting $\Delta E_{S_1-T_1}$. The obtained time constants for the S_1 and T_1 states ($\tau_{S_1} = 35 \pm 4$ ns, $\tau_{T_1} = 1.04 \pm 0.05$ ms) are comparable to those of previously reported TADF processes in photoluminescent copper(I) complexes and purely organic emitters^{12–16}. The extracted singlet–triplet energy splitting ($\Delta E_{S_1-T_1} = 1,652 \pm 32$ cm^{−1}) is in excellent agreement with the value estimated from the emission maxima for the respective fluorescence and phosphorescence spectra measured in solution.

On further cooling to 77 K, the phosphorescence spectrum of $\text{Zr}(\text{MesPDP}^{\text{Ph}})_2$ in frozen 2-MeTHF glasses reveals a hypsochromic shift compared to the fluid solution spectrum (Supplementary Fig. 14). This is attributed to rigidochromism⁴⁰ resulting from different dipole moments in the T_1 state compared to the ground state. This is supported by DFT calculations that predict a dipole moment of 1.7 D for the T_1 state, which shows lower symmetry (C_{2v}) compared to the ground state (D_{2d}), most clearly reflected in a shortening of the Zr–N_{pyridine} bond for one of the two PDP ligands and resulting in a distortion along the z axis of the complex (Supplementary Table 4). This lowering of the molecular symmetry in the T_1 state is best described as an excited-state Jahn–Teller effect due to promotion of an electron to the degenerate set of LUMOs. In addition to the hypsochromic shift, the frozen solution emission spectrum exhibits a smaller line width than the solution spectrum, revealing additional fine structure in the phosphorescence with peak maxima at 620 nm and 670 nm. The photoluminescence decay kinetics measured at 77 K are wavelength-independent and feature a lifetime of $\tau_p = 9.7$ ms (Supplementary Fig. 15).

TA spectroscopy. The successful application of a model assuming thermal equilibrium between the S_1 and T_1 states suggested rapid population and depopulation of the triplet excited state compared to direct radiative and non-radiative depopulation of the lowest singlet excited state (S_1). Rapid intersystem crossing in $\text{Zr}(\text{MesPDP}^{\text{Ph}})_2$ is supported by the absence of prompt fluorescence and strictly single-exponential emission decay at all temperatures, indicating quantitative depopulation of the S_1 state after photoexcitation. To measure the intersystem crossing time constant and gain fundamental insight into the excited-state dynamics, femtosecond TA (fs-TA) spectroscopy studies were conducted in THF solutions at room temperature. The transient difference spectra recorded following pulsed excitation at 480 nm show four distinct features at short delay times that can be characterized as excited-state absorption with a maximum at 723 nm, stimulated emission with a minimum at 609 nm and two excited-state absorption features at 566 and 525 nm. Within the first 5 ps, the transient difference spectra undergo only minor changes that are most clearly observable as an increase of the excited-state absorption signal at 566 nm and a slight decrease of the excited-state absorption feature at 723 nm (Fig. 4). We interpret this spectral evolution as excitation of the molecule to the S_1 state ($^1\text{IL}/^1\text{LMCT}$) followed by internal conversion due to minor changes in the molecular structure of S_1 . These geometric changes are probably the result of a symmetry lowering from D_{2d} to C_{2v} due to an excited-state Jahn–Teller effect. Similar to the distortions calculated for the T_1 state, a significant contraction of one Zr–N_{pyridine} bond was observed by TD-DFT excited-state geometry optimizations (Supplementary Table 4). Over the next 100 ps, the S_1 state converts to a long-lived excited state that persists over the entire delay time in the fs-TA experiments (Fig. 4). Additional μs -TA spectroscopic measurements confirmed that this excited state decays back to the ground state with a time constant consistent with the lifetime determined using time-dependent emission spectroscopy and is therefore assigned as the T_1 excited state ($^3\text{IL}/^3\text{LMCT}$). The difference

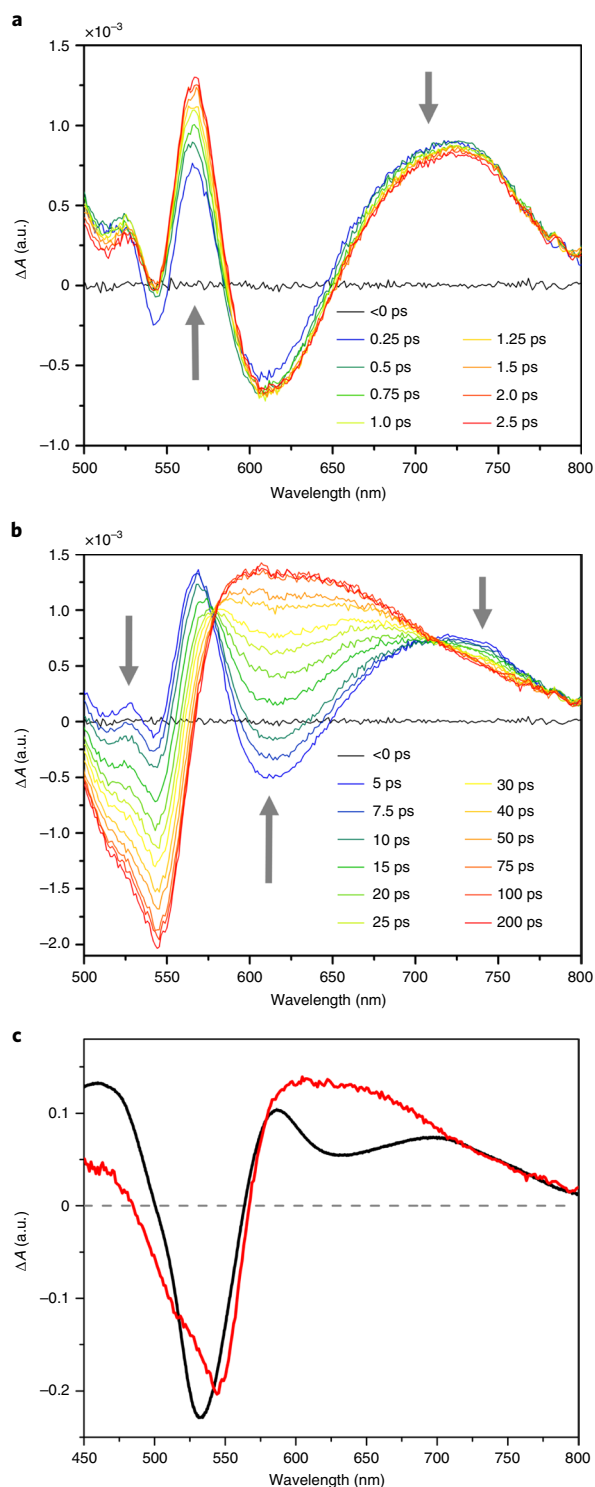


Fig. 4 | Femtosecond TA spectroscopic data revealing the excited-state dynamics of $\text{Zr}(\text{MesPDPPh})_2$. **a**, Time-resolved transient difference spectra recorded at selected delay times up to 2.5 ps after pulsed laser excitation at 480 nm. The subtle changes in the transient difference spectra during this time interval are consistent with a structural reorganization in the S_1 excited state. **A**, absorption. **b**, Time-resolved transient difference spectra associated with the $S_1 \rightarrow T_1$ intersystem crossing process. The transient difference spectrum of the T_1 state, shown in red, persists over the full delay time of the TA experiment (7 ns). **c**, Comparison of the experimental (200 ps, red) and redox-based calculated (black) transient difference spectra. The excellent agreement between the two spectra highlights the charge transfer character of the long-lived T_1 excited state.

absorption spectrum of the T_1 state shows a broad $T_1 \rightarrow T_n$ excited-state absorption feature ranging from 565 to 800 nm, overlapping with a strong ground-state bleach below 565 nm with a minimum at 545 nm. The spectral evolution from S_1 to T_1 exhibits two well-defined isosbestic points at 578 and 711 nm, indicating intersystem crossing that completely outcompetes direct S_1 to S_0 relaxation. The shape of the T_1 difference absorption spectrum after 200 ps could be approximated by a combination of the electronic absorption spectra of the oxidized and reduced species and subsequent subtraction of the ground-state spectrum with a scaling factor of 0.8 (Fig. 4). The success of this approach⁴¹ highlights the charge transfer character of the excited state, which is also supported by DFT-calculated difference density maps for the first four states (Supplementary Fig. 39).

Kinetic modelling of the time-dependent TA spectroscopic data with global analysis using a three-state model yielded approximate time constants of $\tau_{IC} = 1.0$ ps and $\tau_{ISC} = 12.3$ ps for the S_1 internal conversion process and $S_1 \rightarrow T_1$ intersystem crossing, respectively, and permitted the extraction of the individual TA spectral signatures of each of the three components (Supplementary Fig. 18). By combining the value for intersystem crossing with the room-temperature equilibrium constant between S_1 and T_1 , $K_{S_1-T_1}$, derived from $\Delta E_{S_1-T_1}$, the time constant for reverse intersystem crossing was calculated to be $\tau_{ISC} = 41.2$ ns. In agreement with the assumed fast equilibrium model between S_1 and T_1 , both τ_{ISC} and τ_{ISC} are several orders of magnitude faster than the corresponding relaxation lifetimes τ_{S_1} and τ_{T_1} , respectively. Taken together, the kinetic data extracted via temperature-dependent emission studies and TA spectroscopy allowed the construction of a detailed kinetic model of the excited-state dynamics in $\text{Zr}(\text{MesPDPPh})_2$, consistent with TADF (Fig. 5).

Photoredox catalytic applications. The long excited-state lifetime and improved redox properties of $\text{Zr}(\text{MesPDPPh})_2$ suggested it may serve as an earth-abundant photocatalyst in a variety of photoredox reactions (Fig. 6). Due to the stability of the photosensitizer, reactions using air- and moisture-stable reagents can be set up under benchtop conditions without the need for dry solvents or substrates. To prevent deleterious singlet oxygen formation in the presence of air, independently detected by $^1\text{O}_2$ phosphorescence in the near-infrared and trapping of $^1\text{O}_2$ with 1,3-diphenylisobenzofuran (Supplementary Figs. 25 and 26), all reactions were operated under an inert atmosphere. In contrast to our first-generation photosensitizer, $\text{Zr}(\text{MePDPPh})_2$, the bulky second-generation complex $\text{Zr}(\text{MesPDPPh})_2$ exhibits excellent functional group tolerance, including more acidic functionalities such as alcohols and carboxylic acids. As a further improvement, the excited state of $\text{Zr}(\text{MesPDPPh})_2$ can undergo both reductive and oxidative quenching, as demonstrated by Stern–Volmer analysis in the presence of sacrificial electron donors and acceptors, respectively (Supplementary Fig. 24). The sampled reactions cover net oxidative, reductive and redox neutral transformations and excited-state reactivity involving energy transfer as well as oxidative and reductive quenching (Fig. 5). Notably, the isomeric ratio of *Z*- and *E*-stilbene at the photostationary state of the photoisomerization reaction is consistent with the energy of the T_1 state of $\text{Zr}(\text{MesPDPPh})_2$ (1.94 eV) determined from the phosphorescence maximum at -130°C (ref. 42). The mechanistic versatility suggests that $\text{Zr}(\text{MesPDPPh})_2$ can be considered a fully functional early-transition-metal substitute for precious-metal photosensitizers^{43,44}.

Conclusions

Our investigations highlight the mostly unexplored potential of zirconium for the development of a new class of early-transition-metal sensitizers featuring long-lived excited states with LMCT contributions and high photoluminescence efficiency, providing an impetus to motivate future studies. Importantly, our results demonstrate that TADF should be seriously considered in future designs of luminescent early-transition-metal complexes. A critical challenge for forthcoming investigations will be the systematic control over the TADF

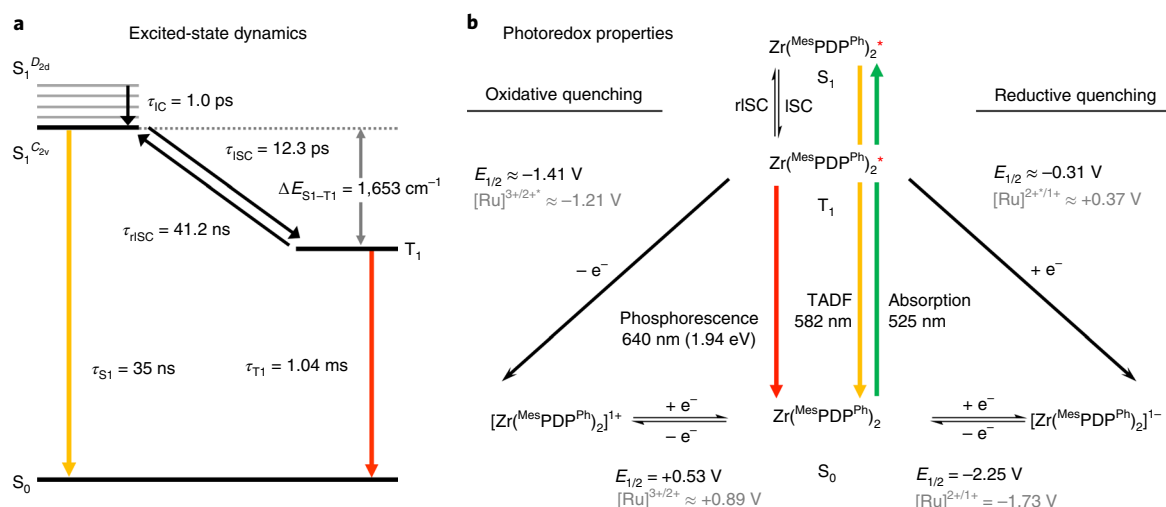


Fig. 5 | Summary of excited-state dynamics and redox potentials of $Zr(MesPDPPh)_2$. **a**, Kinetic model for the thermally activated delayed fluorescence process summarizing parameters determined via temperature-dependent emission and TA spectroscopic studies. **b**, Excited-state redox potentials were estimated from the ground-state redox potentials in THF solution and the triplet state energy obtained from the peak maximum of phosphorescence observed at -130 °C. All potentials are referenced versus the ferrocenium/ferrocene redox couple. For comparison, the corresponding potentials for $[Ru(bpy)_3]^{3+}$ in acetonitrile solution are provided in grey. Values reported versus saturated calomel electrode (SCE) were taken from ref. ⁴⁵ and referenced to ferrocene as outlined in ref. ⁴⁶.

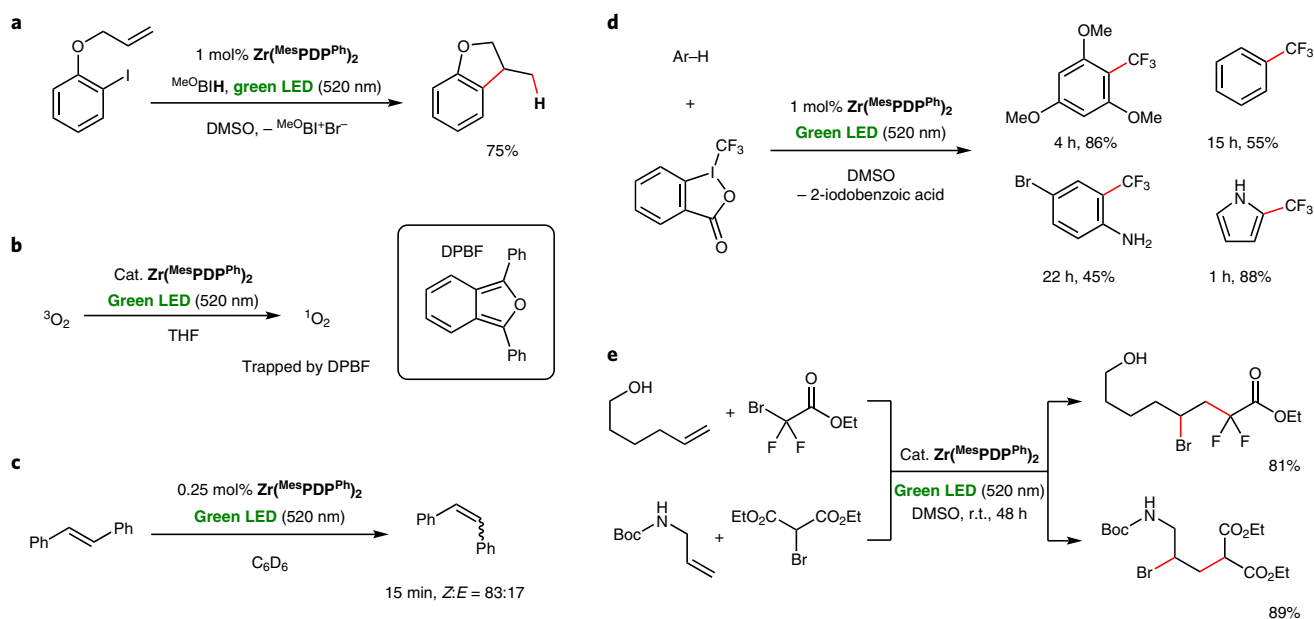


Fig. 6 | Representative examples for photoredox catalytic transformations promoted by $Zr(MesPDPPh)_2$ under visible-light irradiation featuring three distinct mechanisms of substrate activation. **a**, The dehalogenation of an aryl iodide proceeds via reductive quenching of the excited state of $Zr(MesPDPPh)_2$. DMSO, dimethylsulfoxide. **b,c**, The generation of singlet oxygen (**b**) and the isomerization of stilbene (**c**) proceed via excited-state energy transfer. **d,e**, Trifluoromethylation of electron-rich arenes (**d**) and atom transfer radical addition (**e**) are examples proceeding via oxidative quenching of the excited state of $Zr(MesPDPPh)_2$.

lifetime to deliver suitable photosensitizers for different applications. For example, TADF emitters capable of triplet exciton harvesting in energy-efficient OLED applications should exhibit short emission lifetimes. In contrast, photosensitizers for solar energy applications or photocatalysis benefit from long excited-state lifetimes, as displayed by $Zr(MesPDPPh)_2$. An in-depth understanding of the influence of LMCT versus ILCT character on the excited-state dynamics and the energy gap between the S_1 and T_1 states will be critical in this regard.

As exemplified by the unique characteristics of $Zr(MesPDPPh)_2$, earth-abundant early-transition-metal photosensitizers may not only represent a viable low-cost alternative to precious-metal chromophores, but may have the potential to surpass traditional materials in performance-critical parameters such as excited-state lifetime and quantum yield. Most notably, the rigidification of the $Zr(PDP)_2$ framework by the introduction of bulky mesityl substituents resulted in a significant increase of the quantum yield to almost

50%, while maintaining a long excited-state lifetime. In combination with the surprisingly facile oxidative electron transfer chemistry for a complex with d^0 electron configuration, the exceptionally long excited-state lifetime proved to be ideally suited to enabling photoinduced bimolecular reactions under diffusion-controlled conditions, as required in photoredox catalysis and solar fuels photochemistry. The current investigation provides sufficient proof of concept that earth-abundant early-transition-metal LMCT sensitizers can be widely exploited in photoredox catalysis. We expect that the improved stability of $\text{Zr}(\text{MesPDP}^{\text{Ph}})_2$ will also allow a more straightforward exploration of the complex for applications including dye-sensitized solar cells, solar fuels production, photochemical upconversion, organic light-emitting diodes and photodynamic therapy—research areas that have often leveraged precious late-transition-metal-containing sensitizers.

Methods

Preparation of $\text{Zr}(\text{MesPDP}^{\text{Ph}})_2$. Tetrabenzyl zirconium (101 mg, 223 mmol, 0.53 equiv.) and $\text{H}_2\text{MesPDP}^{\text{Ph}}$ (251 mg, 450 mmol, 1.00 equiv.)³⁷ were loaded in a 50 ml thick-walled glass vessel in a glovebox. Approximately 5 ml of toluene was added. The thick-walled vessel was sealed with a PTFE screw cap and heated to 120 °C for 48 h. After cooling to room temperature, the reaction vessel was brought back into the glovebox and additional tetrabenzyl zirconium (101 mg, 223 mmol, 0.53 equiv.) was added. The reaction mixture was heated for another 24 h at 120 °C (at this stage the ligand was fully consumed). The reaction was opened to air, toluene was removed using a rotary evaporator, and the residue was triturated twice with ethyl acetate to give a red solid. The solid was redissolved in dichloromethane/ethyl acetate and filtered through a plug of silica gel. After removal of the solvent, the product was recrystallized by slow evaporation of THF under air. The product was collected as red crystals (yield of 86 mg, 32%) with a melting point of >320 °C. ^1H NMR (400 MHz, C_6D_6 ; δ , ppm): 7.71 (d, $J=8.0$ Hz, 8H), 7.38 (t, $J=8.0$ Hz, 8H), 7.21 (t, $J=8.0$ Hz, 4H), 6.50 (s, 8H, mesityl-CH), 6.49 (d, $J=8.0$ Hz, 4H), 6.25 (t, $J=8.0$ Hz, 2H, para-PyH), 5.95 (s, 4H, pyrroleH), 2.08 (s, 24H, ortho-CH₃), 1.86 (s, 12H, para-CH₃). $^{13}\text{C}\{^1\text{H}\}$ NMR (101 MHz, C_6D_6 ; δ , ppm): 154.59, 142.58, 139.87, 138.39, 138.23, 136.81, 136.01, 131.76, 130.50, 129.71, 128.75, 127.18, 115.58, 112.79, 23.08, 20.94 (one aromatic carbon overlapping). Anal. calcd for $\text{C}_{44}\text{H}_{32}\text{N}_4\text{Zr}\cdot 2\text{C}_4\text{H}_8\text{O}$: C, 79.12; H, 6.36; N, 5.89. Found: C, 78.93; H, 6.35; N, 5.71. Single crystals suitable for X-ray crystallographic analysis were grown from a concentrated THF/Et₂O solution of $\text{Zr}(\text{MesPDP}^{\text{Ph}})_2$ cooled to −35 °C.

Temperature-dependent emission spectroscopy. Steady-state emission spectra from 77 to 340 K were obtained using an Oxford Instruments Optistat DN cryostat with an Edinburgh Instruments FS920 fluorimeter that was equipped with a 450 W Xe arc lamp for excitation source and a Peltier-cooled Hamamatsu R2658P photomultiplier tube (PMT). The Oxford cryostat was also used with an Edinburgh Instruments LP920 laser flash photolysis system for which a tunable Vibrant 355 nm Nd:YAG/OPO system (Opotek) was the excitation source and a Hamamatsu R928 PMT was the detector.

TA spectroscopy. Ultrafast TA measurements were conducted with a 1 kHz Libra, a Ti:sapphire regenerative amplifier system (Coherent Libra), which produces a ~800 nm pulse with ~45 fs temporal resolution with ~4 W power. Using a beamsplitter, the output of the Libra was separated into pump and probe beam paths. The pump beam was directed to an optical parametric amplifier (Light Conversion OPerA). The optical parametric amplifier converts 800 nm Libra output into 480 nm to excite the IL/LMCT transition of $\text{Zr}(\text{MesPDP}^{\text{Ph}})_2$. The beams were directed to the commercial TA spectrometers. We used Helios (Ultrafast System) and EOS (Ultrafast systems) for fs- and μs -TA, respectively. A visible-light continuum, in the ~400–800 nm spectral region, was generated by focusing onto Ti:sapphire crystal. Optical filters were integrated in the probe beam path for rejection of the residual, unamplified, 800 nm radiation. TA measurements were conducted under the magic angle condition where polarization of the probe is 54.7° relative to the pump. Control of the pump and probe polarizations was achieved with two sets of $\lambda/2$ waveplate and polarizer combinations placed in both pump (before the sample) and probe (before continuum generation) beam paths.

Set-up for photoreactions. All photoreactions were performed using commercially available LED light strips with an emission maximum at 520 nm. Constant room-temperature conditions were maintained using a jacketed glass beaker with water cooling or fan. Experimental details for each reaction are provided in the Supplementary Information.

Online content

Any Nature Research reporting summaries, source data, extended data, supplementary information, acknowledgements, peer review information; details

of author contributions and competing interests; and statements of data and code availability are available at <https://doi.org/10.1038/s41557-020-0430-7>.

Received: 20 August 2019; Accepted: 24 January 2020;

Published online: 16 March 2020

References

- Nazeeruddin, M. K., Baranoff, E. & Grätzel, M. Dye-sensitized solar cells: a brief overview. *Sol. Energy* **85**, 1172–1178 (2011).
- Hagfeldt, A., Boschloo, G., Sun, L., Kloo, L. & Pettersson, H. Dye-sensitized solar cells. *Chem. Rev.* **110**, 6595–6663 (2010).
- Ashford, D. L. et al. Molecular chromophore–catalyst assemblies for solar fuel applications. *Chem. Rev.* **115**, 13006–13049 (2015).
- Xuan, J. & Xiao, W.-J. Visible-light photoredox catalysis. *Angew. Chem. Int. Ed.* **51**, 6828–6838 (2012).
- Tucker, J. W. & Stephenson, C. R. J. Shining light on photoredox catalysis: theory and synthetic applications. *J. Org. Chem.* **77**, 1617–1622 (2012).
- Prier, C. K., Rankic, D. A. & MacMillan, D. W. C. Visible light photoredox catalysis with transition metal complexes: applications in organic synthesis. *Chem. Rev.* **113**, 5322–5363 (2013).
- Monro, S. et al. Transition metal complexes and photodynamic therapy from a tumor-centered approach: challenges, opportunities, and highlights from the development of TLD1433. *Chem. Rev.* **119**, 797–828 (2019).
- Yersin, H., Rausch, A. F., Czerwieniec, R., Hofbeck, T. & Fischer, T. The triplet state of organo-transition metal compounds. Triplet harvesting and singlet harvesting for efficient OLEDs. *Coord. Chem. Rev.* **255**, 2622–2652 (2011).
- Xu, H. et al. Recent progress in metal–organic complexes for optoelectronic applications. *Chem. Soc. Rev.* **43**, 3259–3302 (2014).
- Dias, F. B., Penfold, T. J., Berberan-Santos, M. N. & Monkman, A. P. Photophysics of thermally activated delayed fluorescence in organic molecules. *Methods Appl. Fluoresc.* **5**, 012001 (2017).
- Li, G., Zhu, Z.-Q., Chen, Q. & Li, J. Metal complex based delayed fluorescence materials. *Org. Electron.* **69**, 135–152 (2019).
- Uoyama, H., Goushi, K., Shizu, K., Nomura, H. & Adachi, C. Highly efficient organic light-emitting diodes from delayed fluorescence. *Nature* **492**, 234–238 (2012).
- Penfold, T. J., Dias, F. B. & Monkman, A. P. The theory of thermally activated delayed fluorescence for organic light emitting diodes. *Chem. Commun.* **54**, 3926–3935 (2018).
- Kirchhoff, J. R. et al. Temperature dependence of luminescence from $\text{Cu}(\text{NN})_2^+$ systems in fluid solution. Evidence for the participation of two excited states. *Inorg. Chem.* **22**, 2380–2384 (1983).
- Peltier, J. L. et al. Eliminating nonradiative decay in Cu(I) emitters: 99% quantum efficiency and microsecond lifetime. *Science* **363**, 601–606 (2019).
- Czerwieniec, R., Leitl, M. J., Homeier, H. H. H. & Yersin, H. Cu(I) complexes—thermally activated delayed fluorescence. Photophysical approach and material design. *Coord. Chem. Rev.* **325**, 2–28 (2016).
- Wenger, O. S. Photoactive complexes with earth-abundant metals. *J. Am. Chem. Soc.* **140**, 13522–13533 (2018).
- Harlang, T. C. B. et al. Iron sensitizer converts light to electrons with 92% yield. *Nat. Chem.* **7**, 883–889 (2015).
- Chábera, P. et al. A low-spin Fe(III) complex with 100 ps ligand-to-metal charge transfer photoluminescence. *Nature* **543**, 695–699 (2017).
- Kjær, K. S. et al. Luminescence and reactivity of a charge-transfer excited iron complex with nanosecond lifetime. *Science* **363**, 249–253 (2019).
- Lazorski, M. S. & Castellano, F. N. Advances in the light conversion properties of Cu(I)-based photosensitizers. *Polyhedron* **82**, 57–70 (2014).
- Zhang, Y., Schulz, M., Wächter, M., Karnahl, M. & Dietzek, B. Heteroleptic diimine–diphosphine Cu(I) complexes as an alternative towards noble-metal based photosensitizers: design strategies, photophysical properties and perspective applications. *Coord. Chem. Rev.* **356**, 127–146 (2018).
- Arias-Rotondo, D. M. & McCusker, J. K. The photophysics of photoredox catalysis: a roadmap for catalyst design. *Chem. Soc. Rev.* **45**, 5803–5820 (2016).
- Pfennig, B. W., Thompson, M. E. & Bocarsly, A. B. A new class of room temperature luminescent organometallic complexes: luminescence and photophysical properties of permethylscandocene chloride in fluid solution. *J. Am. Chem. Soc.* **111**, 8947–8948 (1989).
- Paulson, S., Sullivan, B. P. & Caspar, J. V. Luminescent ligand-to-metal charge-transfer excited states based on pentamethylcyclopentadienyl complexes of tantalum. *J. Am. Chem. Soc.* **114**, 6905–6906 (1992).
- Heinselman, K. S. & Hopkins, M. D. Luminescence properties of d^0 metal–imido compounds. *J. Am. Chem. Soc.* **117**, 12340–12341 (1995).
- Loukova, G. V., Huhn, W., Vasiliev, V. P. & Smirnov, V. A. Ligand-to-metal charge transfer excited states with unprecedented luminescence yield in fluid solution. *J. Phys. Chem. A* **111**, 4117–4121 (2007).
- Romain, C. et al. Redox and luminescent properties of robust and air-stable N-heterocyclic carbene group 4 metal complexes. *Inorg. Chem.* **53**, 7371–7376 (2014).

29. Loukova, G. V. & Smirnov, V. A. Phosphorescent ligand-to-metal charge-transfer excited states in the group IVB metallocene triad. *Chem. Phys. Lett.* **329**, 437–442 (2000).
30. Gazi, S. et al. Selective photocatalytic C–C bond cleavage under ambient conditions with earth abundant vanadium complexes. *Chem. Sci.* **6**, 7130–7142 (2015).
31. Zhang, Y., Petersen, J. L. & Milsmann, C. A luminescent zirconium(IV) complex as a molecular photosensitizer for visible light photoredox catalysis. *J. Am. Chem. Soc.* **138**, 13115–13118 (2016).
32. Zhang, Y., Lee, T. S., Petersen, J. L. & Milsmann, C. A zirconium photosensitizer with a long-lived excited state: mechanistic insight into photo-induced single electron transfer. *J. Am. Chem. Soc.* **140**, 5934–5947 (2018).
33. Zhang, Y., Petersen, J. L. & Milsmann, C. Photochemical C–C bond formation in luminescent zirconium complexes with CNN pincer ligands. *Organometallics* **37**, 4488–4499 (2018).
34. Zhang, Y., Akhmedov, N. G., Petersen, J. L. & Milsmann, C. Photoluminescence of seven-coordinate zirconium and hafnium complexes with 2,2'-pyridylpyrrolide ligands. *Chem. Eur. J.* **25**, 3042–3052 (2019).
35. Chan, K.-T. et al. Strongly luminescent tungsten emitters with emission quantum yields of up to 84%: TADF and high-efficiency molecular tungsten OLEDs. *Angew. Chem. Int. Ed.* **58**, 14896–14900 (2019).
36. Zhang, L. L.-M. et al. Core-dependent properties of copper nanoclusters: valence-pure nanoclusters as NIR TADF emitters and mixed-valence ones as semiconductors. *Chem. Sci.* **10**, 10122–10128 (2019).
37. Haakey, B. M., Darmon, J. M., Zhang, Y., Petersen, L. & Milsmann, C. Synthesis and electronic structure of neutral square-planar high-spin iron(II) complexes supported by a dianionic pincer ligand. *Inorg. Chem.* **58**, 1252–1266 (2019).
38. Vernitskaya, T. V. & Efimov, O. N. Polypyrrole: a conducting polymer; its synthesis, properties and applications. *Russ. Chem. Rev.* **66**, 443–457 (1997).
39. Herr, P., Glaser, F., Büldt, L. A., Larsen, C. B. & Wenger, O. S. Long-lived, strongly emissive, and highly reducing excited states in Mo(0) complexes with chelating isocyanides. *J. Am. Chem. Soc.* **141**, 14394–14402 (2019).
40. Lees, A. J. The luminescence rigidochromic effect exhibited by organometallic complexes: rationale and applications. *Comments Inorg. Chem.* **17**, 319–346 (1995).
41. Brown, A. M., McCusker, C. E. & McCusker, J. K. Spectroelectrochemical identification of charge-transfer excited states in transition metal-based polypyridyl complexes. *Dalton Trans.* **43**, 17635–17646 (2014).
42. Hammond, G. S. et al. Mechanisms of photochemical reactions in solution. XXII. Photochemical *cis-trans* isomerization. *J. Am. Chem. Soc.* **86**, 3197–3217 (1964).
43. Larsen, C. B. & Wenger, O. S. Photoredox catalysis with metal complexes made from earth-abundant elements. *Chem. Eur. J.* **24**, 2039–2058 (2018).
44. Hockin, B. M., Li, C., Robertson, N. & Zysman-Colman, E. Photoredox catalysts based on earth-abundant metal complexes. *Catal. Sci. Technol.* **9**, 889–915 (2019).
45. Kalyanasundaram, K. Photophysics, photochemistry and solar energy conversion with tris(bipyridyl)ruthenium(II) and its analogues. *Coord. Chem. Rev.* **46**, 159–244 (1982).
46. Connelly, N. G. & Geiger, W. E. Chemical redox agents for organometallic chemistry. *Chem. Rev.* **96**, 877–910 (1996).
- Publisher's note** Springer Nature remains neutral with regard to jurisdictional claims in published maps and institutional affiliations.
- © The Author(s), under exclusive licence to Springer Nature Limited 2020

Data availability

Crystallographic data for the structure reported in this article have been deposited at the Cambridge Crystallographic Data Centre, under deposition no. [CCDC 1922700](https://www.ccdc.cam.ac.uk/structures/) ($\text{Zr}^{\text{(MePDP)}}_2$). Copies of the data can be obtained free of charge via <https://www.ccdc.cam.ac.uk/structures/>. All remaining data are available in the main text or the Supplementary Information.

Acknowledgements

C.M., Y.Z. and D.C.L. acknowledge West Virginia University and the National Science Foundation (CHE-1752738) for financial support. This work used X-ray crystallography (CHE-1336071) and NMR (CHE-1228336) equipment funded by the National Science Foundation. The WVU High Performance Computing facilities are funded by the National Science Foundation EPSCoR Research Infrastructure Improvement Cooperative Agreement no. 1003907, the state of West Virginia (WVEPSCoR via the Higher Education Policy Commission), the WVU Research Corporation and faculty investments. The temperature-dependent static and time-resolved photoluminescence experiments performed at NC State (F.N.C. and J.M.F.) were supported by the US Department of Energy, Office of Science, Office of Basic Energy Sciences, under award no. DE-SC0011979. G.D.S and T.L. acknowledge the Division of Chemical Sciences, Geosciences and Biosciences, Office of Basic Energy Sciences, of the US Department of Energy through grant no. DE-SC0015429.

Author contributions

Y.Z. synthesized and characterized the compound, performed electrochemical measurements, collected steady-state absorption and emission spectra, conducted the majority of photoredox catalytic reactions, and obtained and analysed all computational data. T.S.L. collected and analysed the TA spectroscopic data. J.M.F. conducted the temperature-dependent emission studies and analysed the corresponding data. D.C.L. performed redox titrations and additional photoredox catalytic reactions. J.L.P. determined the crystal structure. G.D.S., F.N.C. and C.M. directed the project and wrote the manuscript.

Competing interests

The authors declare no competing interests.

Additional information

Supplementary information is available for this paper at <https://doi.org/10.1038/s41557-020-0430-7>.

Correspondence and requests for materials should be addressed to C.M.

Reprints and permissions information is available at www.nature.com/reprints.